Far-infrared detection limits – II. Probing confusion including source confusion

Woong-Seob Jeong,[1,2]★ Chris P. Pearson,[2,3]★† Hyung Mok Lee,[1] Soojong Pak[4] and Takao Nakagawa[2]

[1]*Department of Physics and Astronomy, Seoul National University, Shillim-Dong, Kwanak-Gu, Seoul 151-742, South Korea*
[2]*Institute of Space and Astronautical Science, Japan Aerospace Exploration Agency, Yoshinodai 3-1-1, Sagamihara, Kanagawa 229-8510, Japan*
[3]*ISO Data Centre, European Space Agency, Villafranca del Castillo, PO Box 50727, 28080 Madrid, Spain*
[4]*Department of Astronomy and Space Science, Kyung Hee University, Yongin-Si, Gyeonggi-Do 446-701, South Korea*

ABSTRACT
We present a comprehensive analysis for the determination of the confusion levels for the current and the next generation of far-infrared surveys assuming three different cosmological evolutionary scenarios. We include an extensive model for diffuse emission from infrared cirrus in order to derive absolute sensitivity levels taking into account the source confusion noise due to point sources, the sky confusion noise due to the diffuse emission, and instrumental noise. We use our derived sensitivities to suggest best survey strategies for the current and the future far-infrared space missions *Spitzer*, *AKARI* (*ASTRO-F*), *Herschel* and *SPICA*. We discuss whether the theoretical estimates are realistic and the competing necessities of reliability and completeness. We find the best estimator for the representation of the source confusion and produce predictions for the source confusion using far-infrared source count models. From these confusion limits considering both source and sky confusions, we obtain the optimal, confusion limited redshift distribution for each mission. Finally, we predict the cosmic far-infrared background (CFIRB), which includes information about the number and distribution of the contributing sources.

Key words: methods: observational – ISM: structure – galaxies: evolution – cosmology: observations – infrared: galaxies.

1 INTRODUCTION

The detection limits of space infrared (IR) telescope systems are governed by instrumental, photon and confusion noise sources. The instrumental noise is intrinsic to the detector and electronics system, e.g. readout noise and dark current fluctuations. The photon noise is due to Poissonian fluctuations in the photon counts from the sky-background emission and the telescope thermal emission, which can be reduced by decreasing the telescope temperature. On the other hand, the confusion noise is due to both the superposition of point sources in crowded fields and the brightness fluctuation of extended structures at scales of the order of the telescope beam size. In the far-IR bands, due to the relatively large beam sizes, astronomical observations are mostly affected by the sky confusion due to the Galactic cirrus structure (Gautier et al. 1992) and the source confusion due to the unresolved extragalactic sources.

Though the confusion level is the unavoidable limit for the detection of faint point sources, the source structure below the confusion limit also creates background fluctuation in the observed image. This means that the source distribution can be obtained by measuring the background fluctuation, which results from a convolution of the background sources and the telescope optics (Lagache & Puget 2000b; Matsuhara et al. 2000). After the successful *Infrared Astronomy Satellite* (*IRAS*) mission (Soifer, Houck & Neugebauer 1987), subsequent space IR telescopes, such as the Infrared Space Observatory (*ISO*; Kessler et al. 1996) and *Spitzer* (Gallagher, Irace & Werner 2002; Werner et al. 2004), have increased the levels of sensitivity and spatial resolution at far-IR wavelengths. In addition, the Japanese *AKARI* (formerly known as *ASTRO-F*) satellite was launched successfully on 2006 February 21 (Murakami 1998; Nakagawa 2001; Pearson et al. 2004; Shibai 2004; Pearson et al. in preparation) and will perform an all-sky survey in four far-IR bands with much improved sensitivities, spatial resolutions and wider wavelength coverage than the previous *IRAS* survey over two decades ago. Moreover, within the next decade, the Herschel Space Observatory (*Herschel*; Pilbratt

★E-mail: jeongws@ir.isas.jaxa.jp (W-SJ); cpp@ir.isas.jaxa.jp (CPP)
†Contact for further information (http://www.ir.isas.jaxa.jp/~cpp/astrof/).

2002; Harwit 2004) and the Space Infrared Telescope for Cosmology and Astrophysics (*SPICA*; Nakagawa & SPICA Working Group 2004) will observe the much deeper Universe with large aperture sizes of 3.5 m. In our previous paper (Jeong et al. 2005, hereafter Paper I), we numerically generated a high spatial resolution map of the Galactic cirrus and investigated the effect of sky confusion for current and future space far-IR missions. In addition to the simulated sky confusion noise, this work includes realistic source confusion effects assuming various cosmological evolutionary scenarios. We also obtain the expected cosmic far-infrared background (CFIRB).

The fluctuations in the surface brightness of extended structure on scales smaller than the resolution of the telescope/instrument beam can produce spurious events that can be easily mistaken for genuine point sources, because the existence of a source is usually simply derived from the difference in signal between the on source and some background (off source) position. Such extended structure is observed in wispy neutral interstellar dust in the Milky Way that is heated by the interstellar radiation field and is known as the IR cirrus (Low et al. 1984), and is one of the main noise sources in the far-IR range. Cirrus emission peaks at far-IR wavelengths but was detected in all four *IRAS* bands. There have been realistic estimations of the sky confusion from observational data by *IRAS* and *ISO* (Helou & Beichman 1990; Gautier et al. 1992; Herbstmeier et al. 1998; Kiss et al. 2001; Kiss, Klaas & Lemke 2005; Paper I). The intensity of Galactic cirrus is a function of Galactic latitude and is serious for wavelengths longer than 60 μm. Using high-resolution maps extended from currently available Galactic emission maps, we have estimated the sky confusion noise for various missions, based on fluctuation analysis and detailed photometry over realistically simulated images. In Paper I, we concluded that the sky confusion is expected to be 2 orders of magnitude lower for the next generation of space missions with larger aperture sizes, such as *Herschel* and *SPICA*, but, on the other hand, current 60–90 cm aperture missions, such as *Spitzer* and *AKARI*, will have to endure a sky dominated by confusion noise at long wavelengths (>100 μm). In this paper, we also discuss the composite effect of sky confusion and source confusion from the implementation of a realistic model for the source distribution.

Note that additional components affecting the confusion noise are the presence of faint, unresolved, asteroids and the zodiacal light. Though bright asteroids can be easily rejected via source confirmation between two pointings/scans over the same sky position, faint asteroids may contribute to fluctuations assumed to be from faint galaxies. Although Ábrahám, Leinert & Lemke (1997) found no such fluctuations on small scales from the ISOPHOT (photometer on board the *ISO*) data, more sensitive instruments may detect them. Thus, these two components may show a non-negligible contribution to the far-IR confusion near the ecliptic plane.

This paper is structured as follows. In Section 2, we briefly describe the confusion noise due to sky brightness fluctuations and the source confusion due to extragalactic point sources. We present our source count models including galaxy evolution and the simulated images in Section 3. Based upon the specifications of each IR mission, we estimate the source confusion noise through fluctuation and photometric analyses in Section 4. We present the expected results from our simulations in Section 5. Our conclusions are summarized in Section 6.

Throughout this work, we assume a concordance cosmology of $H_0 = 72 \, \mathrm{km \, s^{-1} \, Mpc^{-1}}$, $\Omega_m = 0.3$ and $\Omega_\Lambda = 0.7$, unless otherwise explicitly stated.

2 CONFUSION DUE TO EXTRAGALACTIC SOURCES

The galaxy confusion limit is defined as the threshold of the fluctuations in the brightness of the sky below which sources cannot be discretely detected in the telescope beam $\theta \sim \lambda/D$, where λ is the observation wavelength and D is the telescope diameter. Thus, the fluctuation noise arises from the same origin as the galaxies that one is aiming to detect. If we assume galaxies are distributed as a power law in flux, S, down to some detection limit S_{lim},

$$N(>S) = N_{\mathrm{lim}} \left(\frac{S}{S_{\mathrm{lim}}} \right)^{-\alpha} , \tag{1}$$

where $N(>S)$ is the number of sources per unit solid angle with flux greater than S, α is the slope of the integral source counts (where $\alpha = 1.5$ for a Euclidean universe) and N_{lim} is the number of sources brighter than S_{lim} per unit solid angle. Assuming that the counts flatten at some faint flux, S_0, i.e. $\alpha(S_0) = 0$, then the intensity of the background (in Jy sr^{-1}) up to some maximum flux, S_{max}, corresponding to these sources is given by

$$I = \int_{S_0}^{S_{\mathrm{max}}} S \frac{dN}{dS} \, dS. \tag{2}$$

The fluctuations contributed by sources below the detection limit S_{lim} are given by the second moment of the differential source counts $dN/dS, \sigma_{\mathrm{sc}}$,

$$\sigma_{\mathrm{sc}}^2 = \int_{S_0}^{S_{\mathrm{lim}}} S^2 \frac{dN}{dS} \, dS. \tag{3}$$

Assuming the power-law distribution of sources given in equation (1), equation (3) can be evaluated to give

$$\sigma_{\mathrm{sc}}^2 = N_{\mathrm{lim}} \, S_{\mathrm{lim}}^2 \, \frac{\alpha}{2 - \alpha} \left[1 - \left(\frac{S_0}{S_{\mathrm{lim}}} \right)^{2-\alpha} \right]. \tag{4}$$

For the Euclidean case, the dominant sources contributing to the background intensity are those just below the detection limit S_{lim} (Lagache & Puget 2000b; Matsuhara et al. 2000). However, the strong evolution detected in the galaxy population steepens the source counts and produces super-Euclidean slopes ($\alpha > 1.5$) and the sources around the detection limit also contribute significantly to the fluctuations in the background intensity.

Rigorous theoretical definitions of confusion have been presented by Scheuer (1957) and Condon (1974). Hogg (2001) has highlighted more practical aspects of galaxy confusion noise. An analytical derivation broadly following Franceschini et al. (1989) is given below. Note that the clustering of sources will complicate the confusion noise (e.g. as in the case of radio sources, Condon 1974), although here, for clarity, we do not treat this effect. Some authors (Franceschini et al. 1989; Negrello et al. 2004; Takeuchi & Ishii 2004) have investigated the effect of the clustering of sources on the confusion limit. They found that clustering possibly increases the level of the source confusion by 10 per cent for *AKARI* mission (Takeuchi & Ishii 2004) and by 10 ∼ 15 per cent for *Spitzer* and *Herschel* missions (Negrello et al. 2004) in the far-IR range.

Assuming that the sources are distributed randomly over the sky described by a power-law form $N(S) \propto S^{-\alpha}$ and a corresponding differential distribution given by $dN/dS = kS^{-\gamma}$ where $\gamma = \alpha - 1$, the detector response to a source of flux S, at a position (θ, ϕ) from the axis of a detector beam of profile (point spread function, PSF) $f(\theta, \phi)$ is given by $x = S f(\theta, \phi)$. Hence, the mean number of responses with amplitudes between x and $x + dx$ in a solid angle

$d\Omega$ is given by

$$R(x) = \int_{\Omega_b} \frac{n[x/f(\theta, \phi)]}{f(\theta, \phi)} \, d\Omega, \tag{5}$$

where Ω_b is the solid angle of the beam in steradians. Note that for the power-law distribution of sources discussed above, equation (5) can be rewritten as

$$R(x) = kx^{-\gamma} \int_{\Omega_b} f(\theta, \phi)^{\gamma-1} \, d\Omega = kx^{-\gamma} \Omega_e, \tag{6}$$

where $\Omega_e = \int f(\theta)^{\gamma-1} \, d\Omega$ is the effective beam size (Condon 1974). Taking the second moment of the $R(x)$ distribution (the variance) gives the fluctuation of the response, σ_{sc},

$$\sigma_{sc}^2 = \int_0^{x_c} x^2 R(x) \, dx, \tag{7}$$

where x_c is a cut-off response introduced to stop the variance from diverging at bright source fluxes. More practically, the confusion limit x_c (corresponding to a cut-off flux S_c) is set to some factor of the confusion noise such that $x_c = q\sigma_{sc}$, where the factor q (usually chosen values between 3 and 5) limits the largest response included in the evaluation of the confusion noise σ_{sc} (values of ~ 5 are assumed in the calculations of Franceschini et al. 1991). The difference in assuming a cut-off in the response as opposed to a cut-off in the flux is that weak contributions from strong sources are not neglected, as even a strong source far from the axis of the beam may contribute significantly to the PSF of the beam.

Assuming for clarity in the calculations a circular Gaussian beam profile, $f(\Theta) = f[(\theta/\theta_o)^2] = e^{-4(\theta/\theta_o)^2 \ln 2}$ such that $d\Theta = 2\theta \, d\theta/\theta_o^2$ where θ_o is the FWHM of the beam, integrating equation (7) over the solid angle of the beam gives

$$\sigma_c^2(x_c) = \pi\theta_o^2 P(x_c) \tag{8}$$

or

$$\theta_o = \sqrt{\frac{\sigma_c^2}{\pi P(x_c)}}, \tag{9}$$

where P, effectively the power in the fluctuations, is given by

$$P(x_c) = \int_0^{x_c} x^2 \, dx \, n[x/f(\Theta)] e^{4\Theta \ln 2} \, d\Theta. \tag{10}$$

Thus, the confusion limit can be directly related to the FWHM of the instrumental beam. For the simple power-law representation of the distribution of extragalactic sources given previously and the definitions of equations (5) and (6), the confusion limit is given by

$$\sigma_c = \sqrt{\frac{k\Omega_e}{3-\gamma}} \, x_c^{(3-\gamma)/2}. \tag{11}$$

Therefore, the confusion noise limit will be a complex function of the beam size θ_o, the source counts $N(S)$, the cut-off in flux S_c or response x_c and the factor q. For the assumed symmetric Gaussian beam profile, $\sigma_c \propto \theta_o^{2/(\gamma-1)}$.

The confusion due to faint galaxies will be worse at longer wavelengths and smaller telescope diameters. Because the confusion noise is related to the mean number of responses (the source density) and the cut-off response q/x_c, a useful, practical benchmark for the confusion limit can be set by limiting the number of sources per beam before the beam becomes confused. Ideally, the confusion limit would be determined by the flux at which the source density becomes 1 source per beam, although more realistically a limit of between 1/20–1/50 sources per beam (20–50 beams per source) is assumed (e.g. Hogg 2001). Note that this difference is due to the contribution from faint sources undetected below a certain limit.

## 3 THE INPUT CATALOGUES AND SIMULATED IMAGES

Many authors (Condon 1974; Franceschini et al. 1989; Helou & Beichman 1990; Gautier et al. 1992; Herbstmeier et al. 1998; Kiss et al. 2001, 2003; Paper I) have described the source confusion due to extragalactic point sources and the sky confusion due to Galactic cirrus as separate issues because most extragalactic surveys are limited to low background regions. However, in order to cover much larger survey areas, we also naturally have to include the medium-to-high background regions. In addition, because the cirrus structure covers both large and small scales, both of these contributions should be considered together. By using various source distributions and a realistically simulated cirrus background, we address the effects of sky confusion and source confusion simultaneously with a more realistic framework.

3.1 Input catalogues

The input catalogues are prepared using the models of Pearson (2001, hereafter CPP). CPP is a far-IR model based on the *IRAS* colours and luminosity function of galaxies (see also Pearson & Rowan-Robinson 1996). The model incorporates a four-component parametrization of galaxy spectral energy distributions (SEDs) segregated by *IRAS* \ colours (Rowan-Robinson & Crawford 1989). A normal galaxy population modelled on the cool 100/60 μm colours identified with IR cirrus (Low et al. 1984; Efstathiou & Rowan-Robinson 2003). A starburst population based upon the warm 100/60 μm colours of *IRAS* galaxies with the modelled archetypical starburst galaxy M82 as a template SED (Efstathiou, Rowan-Robinson & Siebenmorgen 2000a). An ultraluminous galaxy population (Sanders & Mirabel 1996) representing the high-luminosity tail of the *IRAS* starburst galaxies assumed to have the SED of an archetypical ultraluminous IR galaxy (ULIG) Arp 220 (Efstathiou et al. 2000a). An active galactic nucleus (AGN; Seyfert 1 and 2) population modelled on a 3–30 μm dust torus component (Rowan-Robinson 1995) defined by hot 25/60 μm colours. Though recent *Spitzer* observations showed silicate dust emissions in luminous and low-luminosity AGN (Hao et al. 2005; Siebenmorgen et al. 2005; Sturm et al. 2005), we do not include them. The input SEDs are
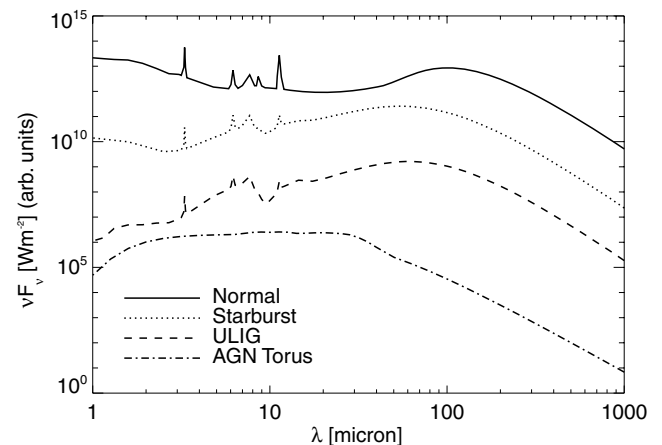
Figure 1. Model input spectral energy distributions used for input catalogues to the simulation. A four-component model comprising a normal galaxy, starburst galaxy, ultraluminous galaxy and AGN dust torus are included. The source spectral energy distributions are based on the models of Efstathiou et al. (2000a), Efstathiou & Rowan-Robinson (2003) and Rowan-Robinson (1995).
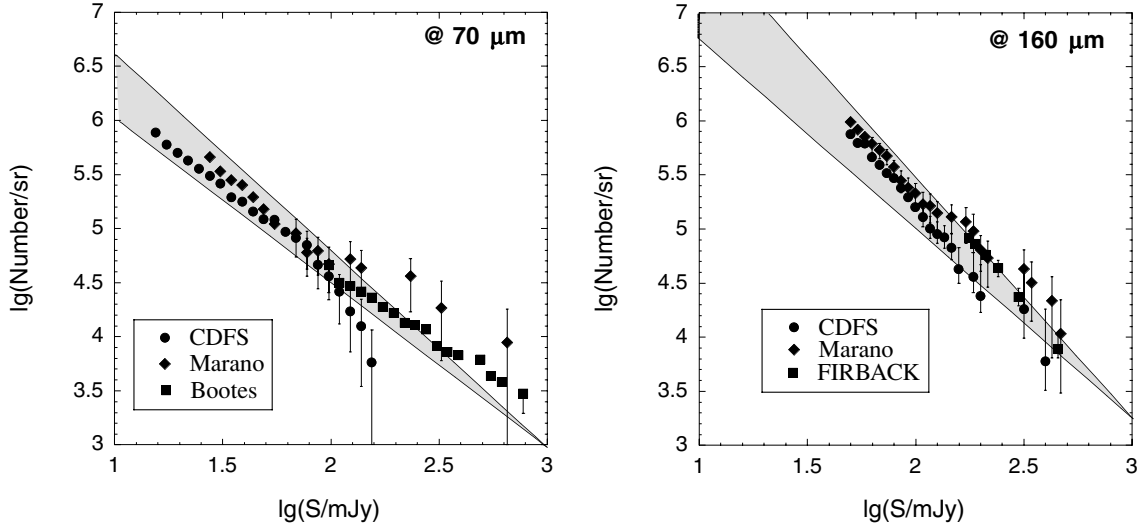
Figure 2. Comparison between source count models and observations for the SW (left) and LW (right) band. All observations except for the FIRBACK field (Dole et al. 2001) were obtained from the Multiband Imaging Photometer for *Spitzer* (MIPS; Rieke et al. 2004) in the *Chandra* Deep Field-South (CDF-S), the Boötes field and Marano field (Dole et al. 2004a). The observational mode (scan map) provides multiple sightings of each source, typically 10 and 60 at 70 μm in the Boötes and CDF-S, respectively. Because of the low redundancy level of the 160 μm data in the Boötes field, Dole et al. (2004a) exclude those data. Upper and lower lines show our burst evolution model and luminosity evolution model, respectively, with the hashed area defining the upper and lower bounds of far-IR source distributions assumed in this work.

shown in Fig. 1. These SEDs have been shown to provide good fits to the SEDs and colours of sources in the *ISO*-ELAIS (European Large Area *ISO* Survey) survey at 6.7, 15, 90 and 170 μm (Rowan-Robinson et al. 2004) and also recently for the first results from the *Spitzer* SWIRE (*Spitzer* Wide-Area Infrared Extragalactic Survey) Legacy survey (Rowan-Robinson et al. 2005).

To produce the input source distributions, we calculate the total number of sources per unit solid angle at observation wavelength, λ_o, down to some flux limit $S_{\lambda o}$:

$$N(S_{\lambda o}) = \int_0^\infty \int_0^{z(L,S)} \phi[L/f(z)] \frac{dV(z)}{dz} e(z) \, d\log L \, dz, \qquad (12)$$

where $f(z)$ and $e(z)$ are evolutionary functions in the luminosity and density of the source population, respectively. The integration is made over the luminosity function (number density of objects as a function of luminosity), $\phi(L)$ and the cosmological volume V, enclosed inside a limiting redshift $z(L, S)$ defined as the redshift at which a source of luminosity, L, falls below the sensitivity, $S(\lambda_o)$.

Luminosity functions, $\phi(L)$, are determined from the All-Sky *IRAS* PSCz (Point Source Catalog Redshift Survey) catalogue at 60 μm by Saunders et al. (2000) for starburst and normal galaxies following colour criteria akin to those of Rowan-Robinson & Crawford (1989). Similarly, the *hot* AGN population is well represented by the 12-μm sample of Rush, Malkan & Spinoglio (1993) using the luminosity function of Lawrence et al. (1986). In addition to the above, following CPP, we utilize a log exponential luminosity function, defined at 60 μm (referred to as the *burst* model), to represent the ULIG population – it was originally implemented to address the paradigms of the strong evolution in the galaxy source counts observed in the mid- to far-IR with the *ISO*, at submillimetre wavelengths with the Submillimetre Common User Bolometer Array (SCUBA) and the detection of the CFIRB at ∼170 μm (Oliver et al. 1997; Smail, Ivison & Blain 1997; Hughes et al. 1998; Kawara et al. 1998; Altieri et al. 1999; Aussel et al. 1999; Flores et al. 1999; Gruppioni et al. 1999; Puget et al. 1999; Biviano et al. 2000; Efstathiou et al. 2000b; Elbaz 2000; Lagache et al. 2000; Matsuhara

et al. 2000; Serjeant et al. 2000; Scott et al. 2002; Meltcalfe et al. 2003). This model was found to provide a good fit to both the number counts and redshift distributions of galaxies from submillimetre to near IR wavelengths as well as the cosmic IR background. To shift the luminosity function from the wavelength at which the luminosity function is defined, λ_{LF}, to the observation wavelength, λ_o, the ratio $L(\lambda_o)/L(\lambda_{LF})$ is obtained via the model template spectra.

We prepare three types of input catalogue and produce many versions of each catalogue to reduce statistical errors.

(i) *No-evolution model*: no evolution is assumed for all galaxy components.

(ii) *Luminosity evolution model*: luminosity evolution is included following Pearson & Rowan-Robinson (1996). Only evolution in the luminosity of the source population is assumed in this scenario. This luminosity evolution follows a parametric form as a function of redshift of $f(z) = (1 + z)^k$, where k is independently defined for each galaxy type to produce the best fits to the far-IR counts.

(iii) *Burst evolution model*: luminosity and density evolution is included following the CPP model. The assumed evolution in both luminosity and density incorporates a burst in a specific redshift range and follows a parametric form as a function of redshift of $f(z)$ and $e(z) = 1 + k \exp[-(z - z_p)^2/2\omega^2]$, where the parameters k, z_p, ω are independently defined for the luminosity and density evolution and galaxy type to produce the best fits to the far-IR counts, and z_p is the characteristic peak redshift in the evolution.

Details of the evolution included in the models can be found in CPP. Fig. 2 shows the evolutionary source count models for the *Spitzer* far-IR galaxy counts at 70 and 160 μm, respectively (Dole et al. 2004a). The two evolutionary models provide reasonable fits and also cover the spread in uncertainty shown in the observations. Therefore, in this work we consider the *burst evolution* and *luminosity evolution* models as upper and lower limits to the numbers of far-IR sources, respectively. We do not attempt to fit the

Table 1. Instrumental parameters for various space missions.

Space mission	Aperture (m)	Central wavelength (μm)		FWHM[a] (arcsec)		Pixel size (arcsec)	
		SW	LW	SW	LW	SW	LW
Spitzer [b]	0.85	70	160	17	35	10	16
AKARI [c]	0.69	75	140	23	44	27	44
Herschel [d]	3.5	70	175[e]	4.3	9.7	3.2	6.4
SPICA	3.5	70	160	4.3	9.7	1.8	3.6

[a]FWHM of the diffraction pattern. [b]Two MIPS bands for the *Spitzer* mission have three bands with central wavelengths of 24, 70 and 160 μm. We use the 70-μm band as the SW band and the 160-μm band as the LW band in this paper. [c]*AKARI*/Far Infrared Surveyor(FIS) has a WIDE-S band in SW and a WIDE-L band in LW. [d]The Photodetector Array Camera and Spectrometer (PACS) has a 'blue' array in two short wavelength bands (centred at 70 and 110 μm) and a 'red' array at longer wavelengths (centred at 175 μm). In this paper, we use only the 70-μm band of the 'blue' array. [b,d]Because one of our motivations in this paper is to compare the confusion limits, we use only common bands among all far-IR bands in the considered space missions. [e]Note that, though the central wavelength of the 'red' array in PACS is 175 μm, our estimated results are for 160 μm. Due to this wider beam, the confusion noise is expected to increase by ∼15 per cent at 175 μm compared with that at 160 μm.
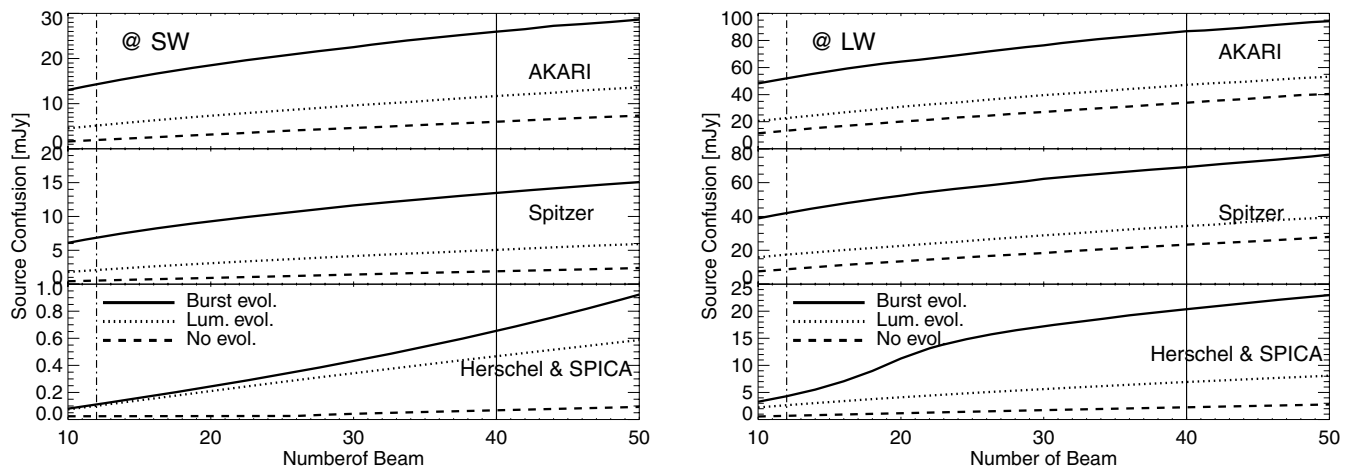
Figure 3. Source confusion with the definition of beams per sources for *AKARI*, *Spitzer*, and *Herschel* & *SPICA* missions. Each line shows the source distribution model used in this paper. The two vertical lines show 12 beams (left) and 40 beams (right) per source, respectively.

mid-near-IR *Spitzer* counts. For specific updated evolutionary models, please see Pearson (2005) and Pearson (in preparation).

3.2 Simulated images

Based upon the three types of input catalogue, we generated simulated images in each band for various space missions. The image size for the distributed source simulation is ∼5.3 deg². In order to check the effect of sky confusion noise, we also include high-resolution cirrus maps whose mean cirrus brightness ranges from 0.3 to 25 MJy sr^{-1} at 100 μm as the background by using the method described in Paper I.

4 SIMULATION RESULTS

As we described in Section 2, there are many definitions for the source confusion. We compare these definitions and propose an appropriate definition for source confusion. In Table 1, we list the basic instrumental parameters of present and future IR space missions: the aperture of the telescope, the central wavelength, FWHM of the beam profile and the pixel size for each detector.

4.1 Definition by 'beams per source'

First, we estimate the source confusion from the classical definition of source confusion, 'beams per source' (sources per beam). Though often cited in the literature as 'sources per beam', we use the term 'beams per source' for our definition of source confusion in order to compare the effect of source confusion according to the different beam sizes for each mission. We check the source confusion by changing the number of beams per source criterion from 10 to 50. Fig. 3 shows the source confusion assuming this definition for each mission and each model. Hogg (2001) showed that 30 beams per source is the minimum photometric criterion where the source counts are steep and suggested 50 beams per source for the definition of source confusion. Rowan-Robinson (2001) adopted

Table 2. Source confusion estimated by the definition of 12 and 40 beams per source.

| Space mission | No evolution (mJy) | | | | | | Luminosity evolution (mJy) | | | | Burst evolution (mJy) | | | |
| | SW | | LW | | SW | | LW | | SW | | LW | | | |
	$12b^a$	$40b^b$	12b	40b	12b	40b	12b	40b	12b	40b	12b	40b		
Spitzer	0.53	1.9	8.8	23	2.1	5.1	17	34	6.9	13	42	69
AKARI^c	1.9	6.0	13	34	5.1	12	23	47	14	26	52	87
Herschel & SPICA	0.014	0.066	0.65	2.1	0.10	0.47	2.6	6.8	0.11	0.65	4.3	20

[a]Source confusion defined by Dole et al. (2004b): flux corresponding to 12 beams per source. [b]Source confusion defined by Rowan-Robinson (2001): flux corresponding to 40 beams per source. [c]Wide-S band for SW and Wide-L band for LW.

40 beams per source. In recent papers, Dole, Lagache & Puget (2003) and Dole et al. (2004b) suggested that source confusion could be defined by a source density criteria, corresponding to ~12 beams per source for the *Spitzer* mission. They have estimated a source confusion limit for the *Spitzer* mission of 3.2 mJy for the short wavelength (SW) band and 40 mJy for the long wavelength (LW) band, respectively. These results are similar to our estimations with the definition of 12 beams per source for the luminosity evolution model in the SW band and for the burst evolution model in the LW band, respectively. These consistences suggest that the source distribution model used for the estimation of the source confusion limit for the case of *Spitzer* (Lagache, Dole & Puget 2003; Lagache et al. 2004) also predicts that a starburst component and ULIG component dominate the SW and LW bands, respectively. In Table 2, we list the source confusion limits estimated by the definition of 12 and 40 beams per source. As seen from Fig. 3, we found that the source confusion did not increase at a constant rate and that the slope of the source confusion slightly varies according to the source distribution model and the resolution of the mission, especially for the burst evolution model. Therefore, we conclude that we can not apply the same definition of 'beams per source' in a generic way for different missions.

4.2 Definition by fluctuation

Another criterion for the quantification of source confusion can be defined by the fluctuation from beam to beam due to the distribution of the point sources (Condon 1974; Franceschini et al. 1989; Vaisanen, Tollestrup & Fazio 2001; Xu et al. 2001). Because the beam size is large and the source counts are steep, the usual definition of 'beams per source' may not be valid in the case of far-IR photometry. For the PSF, we assume an ideal circular aperture Airy pattern corresponding to the aperture size of the telescopes for each mission except for *AKARI* for which we use the theoretical PSFs estimated from the telescope design (Jeong et al. 2003). To visualize the iteration procedure, we plot the $S_{lim}/\sigma_{sc}(S_{lim})$ ratio as a function of S_{lim} for the *Spitzer* and *Herschel & SPICA* missions for the case of the burst evolution model (see Fig. 4). For the SW band of the *Herschel* and *SPCIA* missions, the S_{lim}/σ_{sc} ratio is always greater than 5, which means that we can not obtain a solution for source confusion, even for $q = 5$. Dole et al. (2003) estimated the source confusion with their best estimator for the *Spitzer* mission. With optimized q parameters of 3.8 in the SW band and 6.8 in the LW band, they obtained source confusion limits of 3.2 and 36 mJy at 70 and 160 μm, respectively. Using our source count models and the same q parameters, we obtained the source confusion limits of 3.7 and 21 mJy for the luminosity evolution model and 12 and 60 mJy for the burst evolution model at the same wavelengths. As
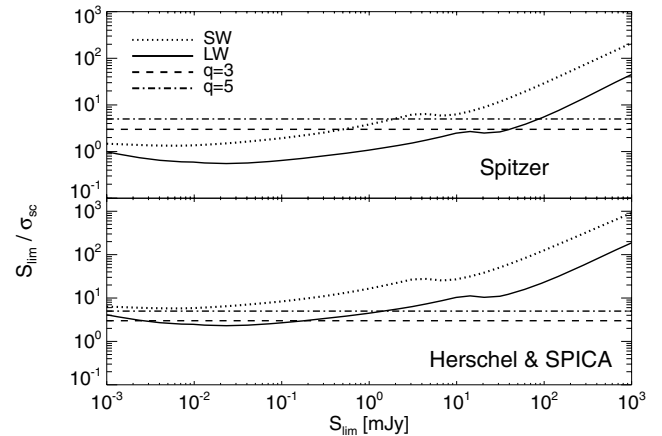
Figure 4. S_{lim}/σ_{sc} ratio as a function of S_{lim} for *Spitzer* (upper) and *Herschel & SPICA* (lower) missions in the case of a burst evolution model. We also plot $S_{lim}/\sigma_{sc} = 3$ (dashed line) and 5 (dashed dotted line). In the case of the *Herschel & SPICA* missions in the SW band, note that S_{lim}/σ_{sc} is always greater than 5, and the plateaus in the SW and LW band are due to the bump seen in the source counts.

we showed in Section 4.1, though the source density of the source count model used in Dole et al. (2003) is similar to the luminosity evolution model in the SW band and the burst evolution model in the LW band, we find that the fluctuation due to distributed sources in the burst evolution model is much stronger than that of the model of Dole et al. (2003). This amount of fluctuation may degrade the final detection limits.

In Table 3, we list the source confusion limits estimated from the definition by fluctuation for the cases of $q = 3$ and 5. For $q = 5$, there are no solutions for the SW band of the *Herschel & SPICA* missions. Even in the LW band, we could not find a reasonable solution because the estimated source confusion for the two evolutionary models gave identical results. However, when we attempted photometry on the simulated images including the point sources for each source count model, we encountered some limits to the source detection. Therefore, we conclude that we can not apply a constant q to the estimation of source confusion generically for all cases.

4.3 Composite definition by fluctuation and photometry

In an attempt to define the source confusion for all cases, we implement a composite definition by fluctuation and photometry. As a first step, we attempt photometry on the simulated images created

Table 3. Source confusion estimated by the definition of fluctuation with $q = 3$ and 5.

Space mission	No evolution (mJy)				Luminosity evolution (mJy)				Burst evolution (mJy)			
	SW		LW		SW		LW		SW		LW	
	$q = 3$	$q = 5$	$q = 3$	$q = 5$	$q = 3$	$q = 5$	$q = 3$	$q = 5$	$q = 3$	$q = 5$	$q = 3$	$q = 5$
Spitzer	0.065	0.28	3.8	10	0.51	1.9	14	33	0.51	1.9	41	87
AKARI	0.36	1.4	5.6	15	2.4	6.8	20	43	2.4	23	59	115
Herschel & SPICA	–[a]	0.002	0.042	0.34	–	0.006	0.18	1.5	–	–	0.18	1.5

[a]No solution for this case.

from each source count model. The definition of completeness and reliability for quantifying the source detection efficiency is widely used in photometry. The 'completeness' is defined as the fraction of detected sources to the original input catalogue sources and the 'reliability' as the fraction of real sources to all detected sources. For our photometry, we removed the false or spurious detections by comparing the positions of detected sources with those in the input catalogue. The real sources as defined in the reliability, refer to sources of which the measured flux agrees with the input flux to within a 20 per cent error. Note that the reliability at a given flux range is not always higher than the completeness. An excess of sources near the detection limit, or more likely an overestimation of the flux of sources at or near the detection limit, can be caused by a step effect where the underlying, unresolved sources are entering the PSF, affecting the sky-subtraction. We carried out aperture photometry on the simulated images using the SEXTRACTOR software v2.2.2 (Bertin & Arnouts 1996). The most influential parameters are the size of the background mesh and the threshold for the source detection for the aperture photometry. Because the size of the background mesh is related to the range of scales of the background fluctuation, as we set a smaller mesh size, we can detect smaller fluctuation. Therefore, if we use a smaller size of background mesh and thresholds, we obtain many more spurious sources. We set the size of the background mesh to ∼2 times the measuring aperture and the detection threshold as 4, which is optimized for better reliability of the detected sources thus reducing the false detection rate.

As discussed in Section 4.2, we could not use a constant value of q for the estimation of source confusion. Current and future space missions, will detect much fainter sources to higher sensitivity, which means that we will observe high source densities to extremely faint detectable flux levels. Therefore, a significant factor contributing to the source detection comes from both the faint sources below the detection limit and the high source density above or around the detection limit. With this assumption, we include the contributed fluctuations from the sources above the detection limit as well. In order to find the limiting flux affecting the source detection, we use a photometric method on the simulated images. We set the limiting flux S_{lim} in equation (3) to be the flux at which the completeness reaches ∼80 per cent where the completeness level abruptly falls off. We do not use the reliability criterion in this definition because the reliability can be improved by using optimized photometric methods. We also assume that the sources above this flux level do not contribute significantly to the source confusion. We obtain the final source confusion from a 4σ fluctuation in order to compare with the threshold used in the photometry. In Table 4, we list the source confusion limits from our best estimators.

Though we could not obtain the results for the SW band of the *Herschel & SPICA* missions with the original definition of the fluctuation with constant q, we could obtain the results with our

Table 4. Source confusion estimated by the composite definition of both fluctuation and photometry.

Space mission	No evol. (mJy)		Lum. evol. (mJy)		Burst evol. (mJy)	
	SW	LW	SW	LW	SW	LW
Spitzer	0.48	9.4	2.0	23	6.5	66
AKARI	2.0	14	6.3	33	17	87
Herschel & SPICA	0.0095	0.63	0.077	2.2	0.10	4.4

new best estimator. We also found that the source confusion limits by our definition are mostly consistent with a completeness of ∼65 per cent for all missions. Therefore, we conclude that our definition can explain the behaviour of source confusion well in the far-IR range, regardless of individual space mission characteristics.

### 4.4 Predicted confusion limits for current and future missions

In our study of sky confusion in Paper I, we predicted the confusion limits considering both sky confusion due to cirrus structure and source confusion for each mission from a rather simple (power law) source distribution model and plotted the sky confusion levels for an assumed range of average cirrus brightness $\langle B_\lambda \rangle$ in Table 5 (see details in Paper I). Kiss et al. (2005) have also estimated the all-sky cirrus confusion for various IR missions. Fig. 5 shows a comparison of sky confusion between Kiss et al. (2005) and Paper I for the *AKARI* mission at 170 μm. The Kiss et al. (2005) model assumes a linear relationship between the cirrus brightness and sky confusion, it often gives different results in low to medium cirrus brightness.

Because, in general, the cirrus fluctuations are not represented by Gaussian noise, we can not directly sum the two noise contributions (sky confusion and source confusion) for the estimation of the final confusion noise. However, in a recent paper, Héraudeau et al. (2004)

Table 5. Estimated confusion limits due to Galactic cirrus for each mission.

Space mission	Sky Confusion Limits (mJy) for $\langle B_\lambda \rangle$[a]					
	0.5 MJy sr^{-1}		5 MJy sr^{-1}		15 MJy sr^{-1}	
	SW	LW	SW	LW	SW	LW
Spitzer	0.10	7.1	1.2	10	11	19
AKARI	0.73	9.4	5.4	18	27	42
Herschel & SPICA	0.003	0.16	0.027	0.21	0.31	0.37

[a]Mean brightness of cirrus emission.
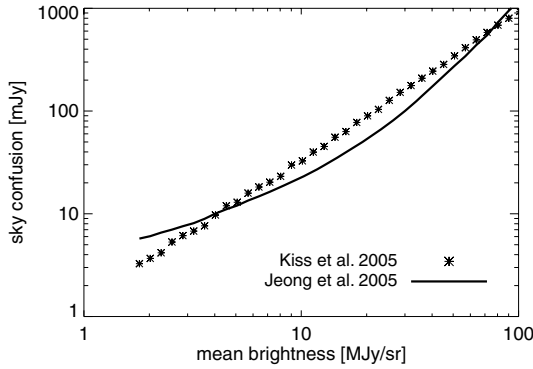
Figure 5. Comparison of sky confusion between Kiss et al. (2005) and Jeong et al. (2005) for the *AKARI* mission at 170 μm. Two results shows significant differences in the range of low and medium cirrus brightness.

found that the distribution of cirrus fluctuation is near-Gaussian, at least at the ISOPHOT 90- and 170-μm spatial frequencies. Thus, we use equation (13) to estimate final confusion limits S_{conf} in this paper by summation of the two confusion noise components:

$$S_{conf} = \sqrt{S_{cc}^2 + S_{sc}^2}, \tag{13}$$

where S_{cc} is the sky confusion limit due to cirrus structure and S_{sc} is the source confusion limit. Fig. 6 shows the final confusion limits due to both sky and source confusion for each mission and each evolutionary model. The sky confusion will be negligible for the *Herschel* and *SPICA* missions even in regions of high cirrus brightness and the dominant confusion contribution is predicted to be the source confusion in high Galactic latitude regions for the purpose of cosmological studies. However, care must be taken when considering the *Spitzer* and *AKARI* missions in the mean cirrus brightness range $\langle B_\lambda \rangle > 20$ MJy sr^{-1} for the LW band. In order to check the effect caused by the combination of both sky and source confusion, we attempt photometry on the simulated images including various cirrus background levels and source count models and we compare them with the photometric results considering only source confusion. These results are presented in Appendix A.

We summarize the confusion limits including both sky and source confusion for each mission in Table 6 for the low cirrus background regions dominated by source confusion. The mean brightness used

in the estimation of sky confusion is 0.5 and 1.0 MJy sr^{-1} for the SW and LW bands, respectively. The sensitivity for the *AKARI* mission is estimated based upon the recent laboratory experiments, and various detector characteristics and observational environments that may affect the final sensitivity (Matsuura et al. 2002; Jeong et al. 2003, 2004; Shirahata et al. 2004). Though the single-scan sensitivity in survey mode of the *AKARI* mission is much lower than the confusion limit, the sensitivity at higher ecliptic latitudes where many scans overlap should approach the confusion limit. For the *Herschel* mission, because the sensitivity is 3 mJy, we expect that most observations in the SW band will be dominated by instrumental noise and those in the LW band will be near the confusion limit. However, the *SPICA* mission will achieve the confusion limit in both bands because it will have a large aperture telescope cooled to very low temperatures (Nakagawa & SPICA Working Group 2004).

The detection limits as a function of integration time can be an important indicator of the confusion level. Based upon recent hardware measurements for the *AKARI* mission and the *Spitzer* results from Dole et al. (2004b), we compare the detection limits as a function of an integration time in Fig. 7. In case of the *AKARI* mission, we also plot the results of different sampling modes for the high background regions. The decreasing component of the noise is the usual behaviour of noise with increasing integration time, while the flattening component is mainly due to the confusion. Because a low cirrus region was assumed in this estimation, the flattening of the noise results from the source confusion. In the SW band, the detection limits are mostly determined by the instrumental noise and the source confusion noise irrespective of the amount of cirrus background except for the very highest cirrus regions, i.e. near the Galactic plane. However, in the LW band, we find that the sky confusion affects the noise level severely in the regions brighter than ~20 MJy sr^{-1} for the *AKARI* mission and ~30 MJy sr^{-1} for the *Spitzer* mission, respectively (see also the plot of confusion limits in Fig. 6). If the different sampling mode for high background regions available for the *AKARI* mission is used, the detection limits are mostly limited by instrumental and photon noises in the SW band unless the exposure time is very long. However, in the LW band, we found that the sky confusion limits compete with the instrumental and photon noises even for short-exposure observations.
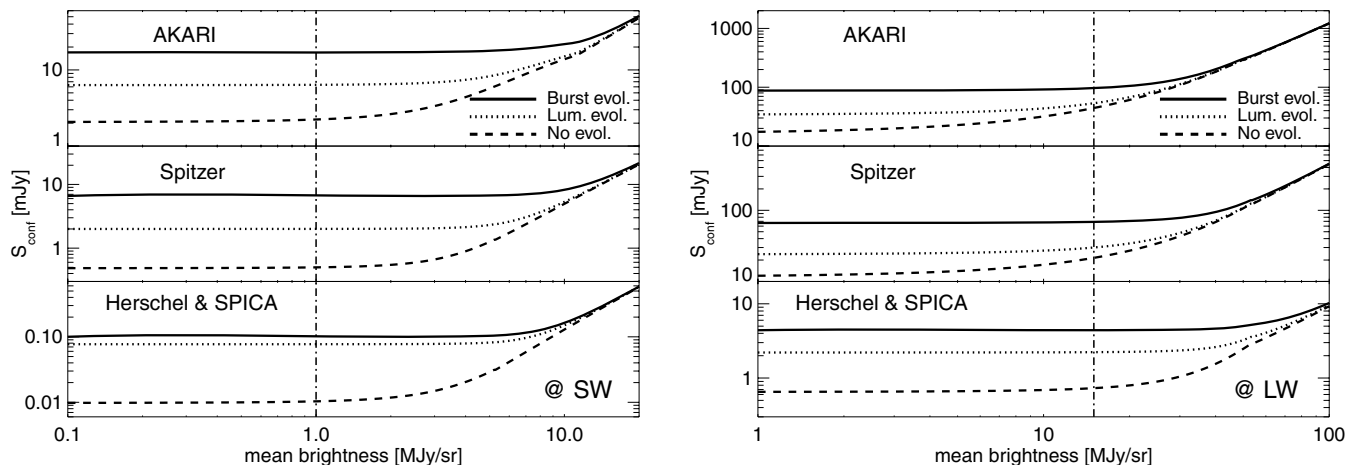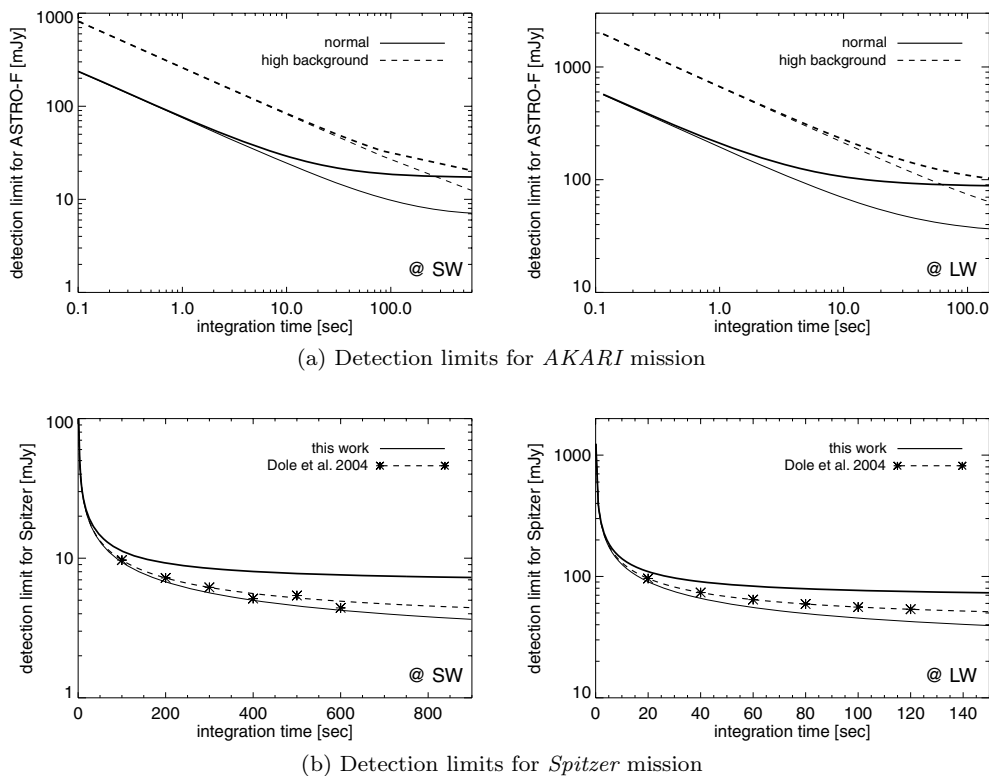

Figure 6. Confusion limits considering both sky confusion and source confusion. The two vertical lines show the mean cirrus brightness 1.0 MJy sr^{-1} for the SW band (left) and 15 MJy sr^{-1} for the LW band (right), respectively. In dark cirrus regions, source confusion is expected to dominate. Note that sky confusion increases as the mean cirrus brightness becomes larger and the source confusion has a constant value irrespective of the mean cirrus brightness.

Table 6. Final confusion limits considering both source confusion and sky confusion.

Space mission	Sensitivity (mJy)		No evolution (mJy)		Luminosity evolution (mJy)		Burst evolution (mJy)	
	SW	LW	SW	LW	SW	LW	SW	LW
Spitzer	6	15	0.49	12	2.0	25	6.6	67
AKARI[a]	12 (200)	12 (400)	2.2	18	6.4	34	17	88
SPICA[b]	3	3	0.010	0.66	0.077	2.3	0.10	4.4
Herschel[c]	3	3	0.010	0.73	0.077	2.6	0.10	5.1

[a]5σ sensitivity for slow scan mode (scan speed, 8 arcsec s^{-1}; reset, 1 s) and survey mode (parenthesized values, one scan). The sensitivity of the survey mode at high ecliptic latitude regions can be improved due to the high redundancy. [b]5σ sensitivity without source confusion and sky confusion. In the case of the *Herschel & SPICA* mission, we commonly use the 5σ sensitivity of the *Herschel* mission (Poglitsch, Waelkens & Geis 2002). [c]Our actual estimations in the LW band are for those in 160 μm. We considered the effect of a wider beam at 175 μm of the LW band.

(a) Detection limits for *AKARI* mission
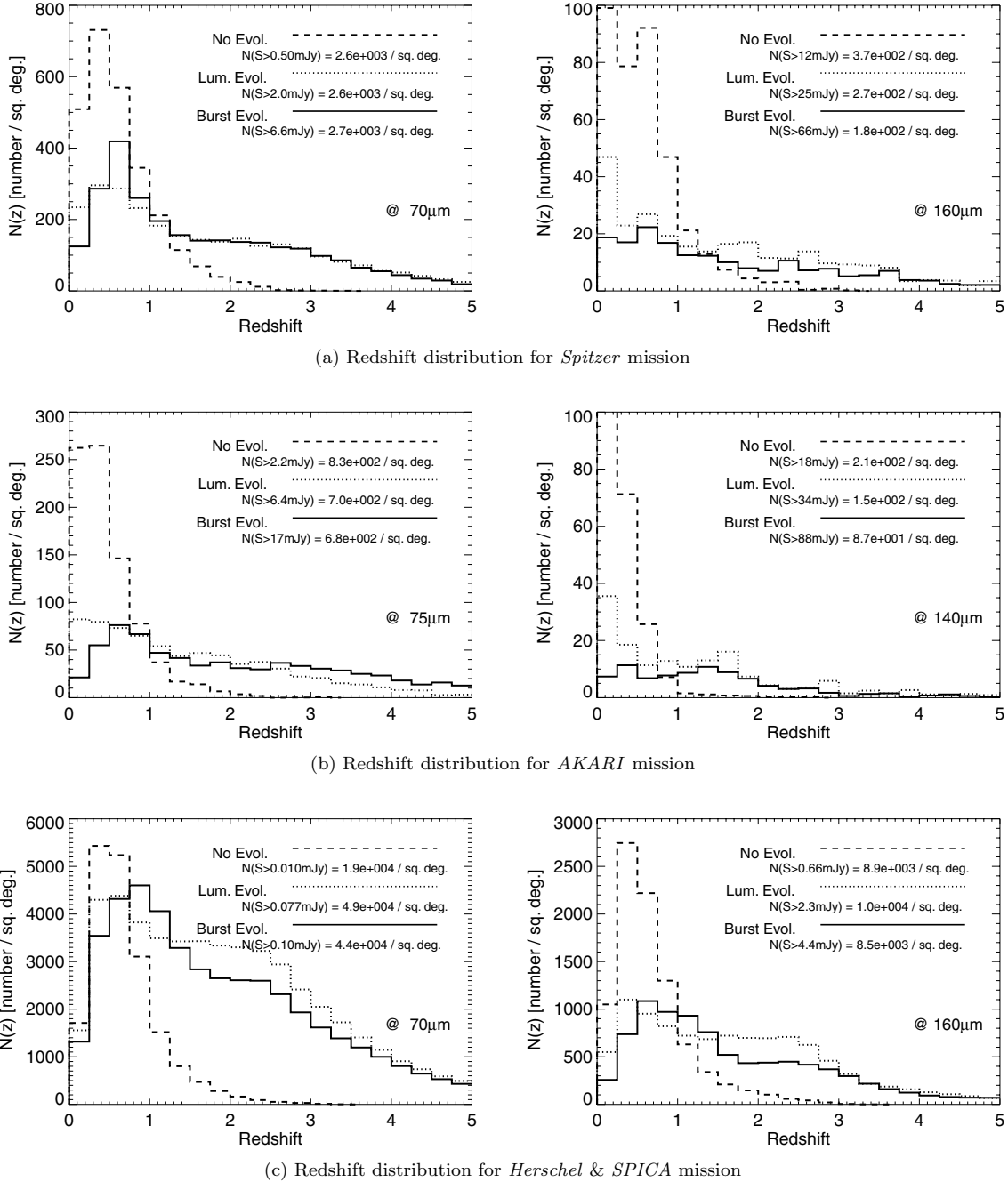

(b) Detection limits for *Spitzer* mission

Figure 7. Comparison of detection limits with integration time for (a) the *AKARI* mission and (b) the *Spitzer* mission. The left panels are for the SW band; the right panels are for the LW band. In the case of the *AKARI* mission, the solid line shows the detection limits over an integration time for normal sampling mode and the dashed line shows those for sampling mode in the high background region to avoid saturation. We plot two evolutionary models. The upper thick line is for the burst evolution model and the lower thin line for the luminosity evolution model. Note that the integration time for a single scan is 0.14 and 0.23 s for the SW band and the LW band, respectively, for *AKARI* and that the integration time is plotted in logarithmic and linear scales for the *AKARI* and *Spitzer* missions, respectively.

5 EXPECTED RESULTS

Based upon two evolutionary (and a no evolution) scenarios of source distributions, we have estimated the expected confusion limits for various IR missions in Section 4.4. The two evolutionary models, the luminosity evolution model and burst evolution model, provide upper and lower limits for the final detection limits. Here, we discuss the results expected from the two evolutionary models from our estimated sensitivities.

5.1 Expected optimal redshift distribution

Once the realistic detection limits have been determined, we can obtain the expected optimal confusion limited redshift distribution from the models. The number–redshift distribution to our limiting flux, S_{lim}, can be extracted directly from our simulated catalogue. In Fig. 8, we show the expected redshift distributions and expected number of sources per square degree for each mission at the predicted confusion limit. We consider this as the optimal redshift

(a) Redshift distribution for *Spitzer* mission

(b) Redshift distribution for *AKARI* mission

(c) Redshift distribution for *Herschel* & *SPICA* mission

Figure 8. Expected optimal redshift distributions for the (a) *Spitzer*, (b) *AKARI* and (c) *Herschel* & *SPICA* missions. The three evolutionary models are shown for the SW and LW bands, respectively, at the confusion limit. These are the optimal distributions for each mission at the absolute sensitivity defined by our analysis.

distribution for each mission. Because a fairly large number of sources below $z < 1.0$ are detected in the LW bands for the no evolution model, the redshift distribution for each mission has a significant difference depending on whether there is evolution or not. Though we can find the peaks in the SW band of the burst evolution model and the LW band of luminosity evolution model for the *Spitzer* and *AKARI* missions, we still have difficulty in finding a significant difference between the two evolutionary scenarios. However, we expect that the large 3.5-m-aperture missions (e.g. *Herschel* and *SPICA*) will have advantages over the 60–90 cm aperture missions (*Spitzer* and *AKARI*) in distinguishing between the

evolutionary scenarios due to the larger numbers of sources detected in the redshift range of 1–3. Because the source confusion should be more severe for stronger evolutionary models, the total number of detected sources in the no evolution model is largest in the LW band except for the *Herschel* and *SPICA* missions.

From Fig. 8, we show that the confusion limit for the *Spitzer* and *AKARI* missions restricts the majority of the sources to redshifts of around or less than unity. For these missions, we could expect of the order of a few tens of sources per redshift bin per square degree out to redshifts of 2–3 (note that the Multiband Imaging Photometer for *Spitzer*, MIPS, 70-μm band is more sensitive in theory but suffers

Table 7. Expected intensity, fluctuation and resolved fraction of CFIRB for each mission. The upper flux is set to be the final confusion limit.

Space mission	Luminosity evolution				Burst evolution			
	SW		LW		SW		LW	
	Intensity (MJy sr^{-1})	Resolved (per cent)	Intensity (MJy sr^{-1})	Resolved (per cent)	Intensity (MJy sr^{-1})	Resolved (per cent)	Intensity (MJy sr^{-1})	Resolved (per cent)
Spitzer	0.063	48	0.33	17	0.12	52	0.69	9
AKARI	0.094	32	0.31	14	0.21	27	0.66	7
Herschel & SPICA	0.013	90	0.16	60	0.015	94	0.21	72

from detector array problems in practice). However, for the *Herschel* and *SPICA* missions, we could expect 500 to thousands of sources per square degree per redshift bin out to redshifts of 2–3. This would allow direct probing of the dusty starburst populations detected at 24 μm with *Spitzer* (Papovich et al. 2004; Rodighiero et al. 2005) and at 850 μm with *SCUBA* (e.g. Chapman 2003) resulting in the construction of much more accurate far-IR luminosity functions out to these redshifts with large-number statistics.

5.2 Expected cosmic far-infrared background

The measurements of the IR background have been carried out in several wavelength bands. Also, there has been rapid progress in resolving a significant fraction of the background with deep galaxy counts at IR wavelengths.

The flux from extragalactic sources below the detection limits creates fluctuations in the background. The CFIRB intensity I_{CFIRB} produced by all sources with the flux below the limiting flux, S_{lim}, is obtained from

$$I_{\mathrm{CFIRB}} = \int_0^{S_{\mathrm{lim}}} S \frac{\mathrm{d}N}{\mathrm{d}S} \, \mathrm{d}S. \qquad (14)$$

In addition, the CFIRB fluctuations P_{CFIRB} from sources with a random distribution below a given detection limit S_{lim} can be estimated as follows:

$$P_{\mathrm{CFIRB}} = \int_0^{S_{\mathrm{lim}}} S^2 \frac{\mathrm{d}N}{\mathrm{d}S} \, \mathrm{d}S. \qquad (15)$$
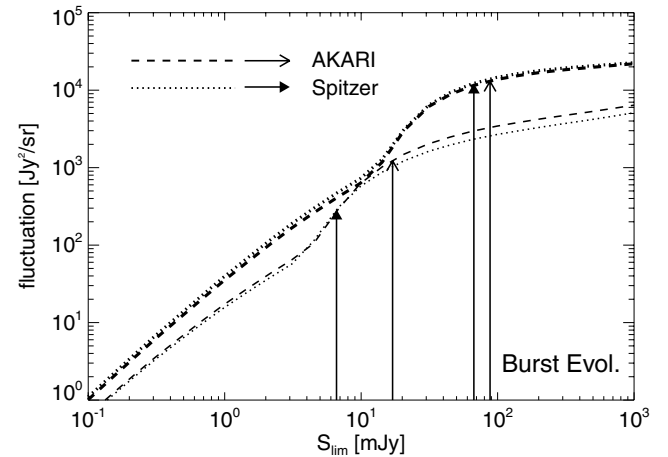
The detection limits S_{lim} can be found in Table 6.

We list the expected CFIRB intensity and resolved fraction for each mission in Table 7. Dole et al. (2004b) predicted that the *Spitzer* mission can resolve 18 per cent of the CFIRB at 160 μm from their source count model. According to our estimation with our source count model, the resolved CFIRB is expected to be 9–17 per cent of the total CFIRB. As shown in Table 7, the *Herschel & SPICA* missions will resolve a much larger fraction of the CFIRB, i.e. 90–94 per cent in the SW band and 60–72 per cent in the LW band, compared with other missions.

Table 8 lists the expected CFIRB fluctuations for each mission. We can not find a significant difference in the fluctuation levels of the *Spitzer* and the *AKARI* missions in the LW band because the detection limits already approach a flux range with a monotonic increase of fluctuation (see Fig. 9 for the burst evolution model). In the far-IR range, Lagache & Puget (2000b) and Matsuhara et al. (2000) have studied the detection of the CFIRB fluctuation with *ISO* data in the Marano 1 region and the Lockman Hole, respectively. For comparison, we list the fluctuation estimated from our model for the *ISO* mission in Table 9. We find that the observed fluctuations are mostly located between the results from our two evolution

Table 8. Expected CFIRB fluctuations for each mission.

Space mission	Luminosity evolution (Jy^2 sr^{-1})		Burst evolution (Jy^2 sr^{-1})	
	SW	LW	SW	LW
Spitzer	35	1600	290	12 000
AKARI	130	1800	1200	13 000
Herschel & SPICA	0.4	120	0.6	290

Figure 9. Expected CFIRB fluctuations for the burst evolution model. Thick lines are for the LW band and thin lines are for the SW band. Two arrows show the expected CFIRB fluctuation corresponding to the detection limits.

models except for the observations at 90 μm. Compared with the model of Lagache et al. (2003), our estimated fluctuations from the burst evolution model are in good agreement with those from their model.

The power spectrum of cirrus emission at high Galactic latitudes ($>80°$) also has a fluctuation of about 10^6 Jy^2 sr^{-1} at 0.01 arcmin^{-1} at 160 μm with a power index of -2.9 ± 0.5. In order to distinguish the CFIRB fluctuations from the observed data that include both CFIRB and cirrus emission effectively, we require an area larger than 115, 125 and 19 arcmin^2 for the *Spitzer*, *AKARI*, and the *Herschel & SPICA* missions, respectively, for the case of the luminosity evolution model. If we adopt the burst evolution model, the minimum required area for the resolution of the estimated power spectrum should increase to 463, 490, 36 arcmin^2 for the *Spitzer*, *AKARI*, and the *Herschel & SPICA* missions, respectively. The shaded area in Fig. 10 covers the fluctuations for both evolutionary models. In

Table 9. Comparison of CFIRB fluctuations for the *ISO* mission.

λ (μm)	θ (arcmin)	S_{max} (mJy)	Observations (Jy^2 sr^{-1})	Predicted[a] (Jy^2 sr^{-1})	Predicted (this work)[b] (Jy^2 sr^{-1})
90	0.4–20	150	$13\,000 \pm 3000$[c]	5300	2100–7200
170	0.6–4	100	7400[d]	12 000	3800–14 000
170	0.6–20	250	$12\,000 \pm 2000$[c]	16 000	5500–18 000

[a]Model from Lagache et al. (2003). [b]The lower limit is estimated from the luminosity evolution model and the upper limit from the burst evolution model. [c]Observational analysis from Matsuhara et al. (2000). [d]Observational analysis from Lagache & Puget (2000b).
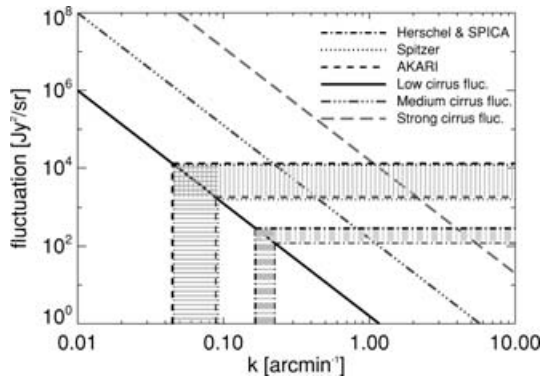
Figure 10. Comparison between expected CFIRB and cirrus fluctuation for each mission in the LW band. The solid line shows the power spectrum of cirrus emission at high Galactic latitude. For comparison, we also plot the power spectrum in medium and high cirrus regions. The shaded area shows fluctuations and corresponding spatial frequencies covering two evolution models at high Galactic latitude for each mission. The lower limit is for luminosity evolution and the upper limit is for burst evolution.
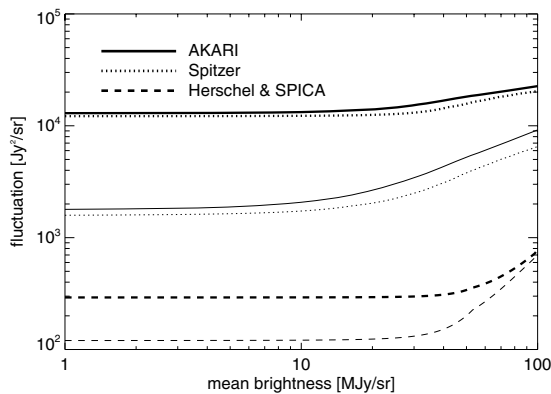
Figure 11. Expected CFIRB fluctuation as a function of cirrus mean brightness in the LW band. The two lines plotted for each mission are for the burst evolution model (upper line) and for the luminosity evolution model (lower line).

this estimation, we do not consider the clustering of extragalactic sources. As sky confusion noise increases in the low Galactic latitude regions, detection limits should also degrade and the CFIRB fluctuation becomes larger (see Fig. 11). As can be seen in Fig. 11, the fluctuations show a monotonic increase to medium cirrus regions. Because the fluctuation power in low Galactic latitude regions should be more than 10^{10} Jy^2 sr^{-1} at 0.01 arcmin^{-1} at 160 μm, it

is difficult to extract the CFIRB fluctuations from the analysis of power spectrum (note that this CFIRB fluctuation is expected to have spatial structure below 1 arcmin^{-1}, see Fig. 10). However, we expect to detect CFIRB fluctuations in most of the low-to-medium cirrus regions.

6 SUMMARY AND CONCLUSIONS

In order to probe the confusion limit for IR observations, we generated source catalogues assuming a concordance (i.e. flat, dark energy dominated) cosmological world model ($H_0 = 72$ km s^{-1} Mpc^{-1}, $\Omega_m = 0.3$ and $\Omega_\Lambda = 0.7$) for two evolutionary scenarios defined as the luminosity evolution model and the burst model following Pearson & Rowan-Robinson (1996) and CPP, respectively. We also considered the sky confusion due to the IR cirrus. Though the sky confusion is not a dominant noise source at high Galactic latitudes, we should take into account the effects of fluctuations of the sky brightness for large-area surveys.

Based upon the fluctuation analysis and photometry on simulated images, we find a composite estimator that represents the source confusion well. From our analysis of source confusion and source distribution models including galaxy evolution, we have estimated final confusion limits of 2.0–6.6 and 25–67 mJy at 70 and 160 μm for the *Spitzer* mission, 6.4–17 and 34–88 mJy at 75 and 140 μm for the *AKARI* mission, 0.077–0.10 and 2.3–4.4 mJy at 70 and 160 μm for the *SPICA* mission, and 0.077–0.10 and 2.6–5.1 mJy at 70 and 175 μm for the *Herschel* mission in low cirrus regions. If the source distribution follows the evolutionary models, the current and planned IR missions will be mostly limited by source confusion. Other components affecting confusion are the fluctuation from the zodiacal light, asteroids and clustering of sources. As yet, the fluctuation of the zodiacal light on small scales has not been observed, although we may expect this information from the current or next generation of space missions. Based upon the number distribution (Tedesco, Cellino & Zappalá 2005) and SED (Müller & Lagerros 1998; Kim et al. 2003) of asteroids, we roughly estimated the effect of source confusion from asteroids. Because the slope of the flux–number distribution is shallower than that of Euclidean space and the number density at any given flux is much smaller than that of our evolutionary source distributions, we expect that the effect from asteroids near the ecliptic plane is not severe, i.e. less than 2 and 0.5 per cent in the SW and LW bands, respectively. The fluctuation from the clustering of sources results in a $10 \sim 15$ per cent increase in the confusion (Takeuchi & Ishii 2004; Negrello et al. 2004) and can be comparable to the sky confusion in regions of medium cirrus brightness in the LW band. This effect of clustering on the confusion should be detectable in the SW band or in regions of low cirrus brightness. Using our study for sky confusion and source

confusion, we have generated all-sky maps for final confusion limits. These maps are shown in Appendix B.

We have also obtained the optimal (confusion limited) redshift distribution from each source count model. The redshift distributions for each mission show significant differences between the no evolution scenario and evolutionary models. However, in order to distinguish between the two evolution models, higher sensitivity/resolution missions (e.g. *Herschel* and *SPICA*) are required compared with the present, relatively low resolution missions. We have estimated that the CFIRB will be resolved to 48–52 and 9–17 per cent at 70 and 160 μm for the *Spitzer* mission, 27–32 and 7–14 per cent at 75 and 140 μm for the *AKARI* mission, and 90–94 and 60–72 per cent at 70 and 160 μm for the *Herschel* & *SPICA* missions. We also found that we can detect the CFIRB fluctuations in most low-to-medium cirrus regions.

ACKNOWLEDGMENT

REFERENCES

Ábrahám P., Leinert C., Lemke D., 1997, A&A, 328, 702
Altieri B. et al., 1999, A&A, 343, L65
Aussel H., Cesarsky C. J., Elbaz D., Starck J. L., 1999, A&A, 342, 313
Bertin E., Arnouts S., 1996, A&AS, 117, 393
Biviano A. et al., 2000, in Mezure A., Le Fevre O., Le Brun V., eds, ASP Conf. Ser. Vol. 200, Clustering at High Redshifts. Astron. Soc. Pac., San Fransisco, p. 101
Chapman S. C., Blain A., Ivison R., Smail I., 2003, Nat, 422, 695
Condon J. J., 1974, ApJ, 188, 279
Dole H. et al., 2001, A&A, 372, 364
Dole H., Lagache G., Puget J.-L., 2003, ApJ, 585, 617
Dole H. et al., 2004a, ApJS, 154, 87
Dole H. et al., 2004b, ApJS, 154, 93
Efstathiou A., Rowan-Robinson M., 2003, MNRAS, 343, 322
Efstathiou A., Rowan-Robinson M., Siebenmorgen R., 2000a, MNRAS, 313, 734
Efstathiou A. et al., 2000b, MNRAS, 319, 1169
Elbaz D., 2000, in Lemke D., Stickel M. K., eds, *ISO* Surveys of a Dusty Universe. Springer-Verlag, Berlin, p. 121
Fixsen D. J., Dwek E., 2002, ApJ, 578, 1009
Flores H. et al., 1999, A&A, 343, 389
Franceschini A., Toffolatti L., Danese L., De Zotti D., 1989, ApJ, 344, 35
Franceschini A., Toffolatti L., Mazzei P., Danese L., De Zotti D., 1991, A&AS, 89, 285
Gallagher D. B., Irace W. R., Werner M. W., 2002, in Mather J. C., ed., Proc. SPIE Vol. 4850, IR Space Telescopes and Instruments. SPIE, Bellingham, WA, p. 17
Gautier T. N. III, Boulanger F., Pérault M., Puget J. L., 1992, AJ, 103, 1313
Gruppioni C. et al., 1999, MNRAS, 305, 297
Hao L. et al., 2005, ApJ, 625, L75
Harwit M., 2004, Adv. Space Res., 34, 568
Helou G., Beichman C. A., 1990, Proc. of the 29th Liege International Astrophysical Coll. ESA Publications Division, Noordwijk, p. 117
Héraudeau Ph. et al., 2004, MNRAS, 354, 924
Herbstmeier U. et al., 1998, A&A, 332, 739
Hogg D., 2001, AJ, 121, 1207
Hughes D. et al., 1998, Nat, 394, 241
Jeong W.-S. et al., 2003, PASJ, 55, 717
Jeong W.-S. et al., 2004, Adv. Space Res., 34, 573
Jeong W.-S., Lee H. M., Nakagawa T., Kwon S. M., Pearson C. P., White G. J., 2005, MNRAS, 357, 535 (Paper I)
Kawara K. et al., 1998, A&A, 336, L9
Kessler M. F. et al., 1996, A&A, 315, 27
Kim S., Lee H. M., Nakagawa T., Hasegawa S., 2003, J. Korean Astron. Soc., 36, 21
Kiss Cs., Ábrahám P., Klaas U., Juvela M., Lemke D., 2001, A&A, 379, 1161
Kiss Cs., Abraham P., Klaas U., Lemke D., Héraudeau Ph., del Burgo C., Herbstmeier U., 2003, A&A, 399, 177
Kiss Cs., Klaas U., Lemke D., 2005, A&A, 430, 343
Lagache G., Puget J. L., 2000b, A&A, 355, 17
Lagache G., Haffner L. M., Reynolds R. J., Tufte S. L., 2000, A&A, 354, 247
Lagache G., Dole H., Puget J. L., 2003, MNRAS, 338, 555
Lagache G. et al., 2004, ApJS, 154, 112
Lawrence A., Walker D., Rowan-Robinson M., Leech K. J., Penston M. V., 1986, MNRAS, 219, 687
Low F. J. et al., 1984, ApJ, 278, L19
Matsuhara H. et al., 2000, A&A, 361, 407
Matsuura S. et al., 2002, in Mather J. C., ed., Proc. SPIE Vol. 4850, IR Space Telescopes and Instruments. SPIE, Bellingham, WA, p. 902
Metcalfe L. et al., 2003, A&A, 407, 791
Müller T. G., Lagerros J. S. V., 1998, A&A, 338, 340
Murakami H., 1998, in Bely P. Y., Breckinridge J. B., eds, Proc. SPIE Vol. 3356, IR Space Telescopes and Instruments. SPIE, Bellingham, WA, ¨ p. 471
Nakagawa T., 2001, in Pilbratt G. L., Cernicharo J., Heras A. M., Prusti T., Harris R., eds, ESA SP-460, The Promise of the Herschel Space Observatory. ESA Publications Division, Noordwijk, p. 67
Nakagawa T., SPICA Working Group, 2004, Adv. Space Res., 34, 645
Negrello M., Magliocchetti M., Moscardini L., De Zotti G., Granato G. L., Silva L., 2004, MNRAS, 352, 493
Oliver S. J. et al., 1997, MNRAS, 289, 471
Papovich C. et al., 2004, ApJS, 154, 70
Pearson C. P., 2001, MNRAS, 325, 1511 (CPP)
Pearson C. P., 2005, MNRAS, 358, 1417
Pearson C. P., Rowan-Robinson M., 1996, MNRAS, 283, 174
Pearson C. P., Matsuhara H., Onaka T., Watarai H., Matsumoto T., 2001, MNRAS, 324, 999
Pearson C. P. et al., 2004, MNRAS, 347, 1113
Pilbratt G. L., 2002, in Mather J. C., ed., Proc. SPIE Vol. 4850, IR Space Telescopes and Instruments. SPIE, Bellingham, WA, p. 586
Poglitsch A., Waelkens C., Geis N., 2002, in Mather J. C., ed., Proc. SPIE Vol. 4850, IR Space Telescopes and Instruments. SPIE, Bellingham, WA, p. 662
Puget J. L. et al., 1999, A&A, 345, 29
Rieke G. H. et al., 2004, ApJS, 154, 25
Rodighiero G. et al., 2005, MNRAS, astro-ph/0511563
Rowan-Robinson M., 1995, MNRAS, 272, 737
Rowan-Robinson M., 2001, ApJ, 549, 745
Rowan-Robinson M., Crawford P., 1989, MNRAS, 238, 523
Rowan-Robinson M. et al., 2004, MNRAS, 351, 1290
Rowan-Robinson M. et al., 2005, AJ, 129, 1183
Rush B., Malkan M., Spinoglio L., 1993, ApJS, 89, 1
Sanders D. B., Mirabel I. F., 1996, ARA&A, 34, 725
Saunders W., Rowan-Robinson M., Lawrence A., Efstathiou G., Kaiser N., Ellis R. S., Frenk C. S., 1990, MNRAS, 242, 318
Saunders W. et al., 2000, MNRAS, 317, 55
Scheuer P. A., 1957, Proc. Cambridge Phil. Soc., 53, 764
Scott S. E. et al., 2002, MNRAS, 331, 817
Serjeant S. B. G. et al., 2000, MNRAS, 316, 768
Shibai H., 2004, Adv. Space Res., 34, 589
Shirahata M. et al., 2004, in Mather J. C., ed., Proc. SPIE Vol. 5487, Optical, Infrared, and Millimeter Space Telescopes. SPIE, Bellingham, WA, p. 369

Siebenmorgen R., Haas M., Krügel E., Shultz B., 2005, A&A, 436, L5

Smail I., Ivison R. J., Blain A. W., 1997, ApJ, 490, L5

Soifer B.T., Houck J. R., Neugebauer G., 1987, ARA&A, 25, 187

Sturm E. et al., 2005, ApJ, 629, L21

Takeuchi T. T., Ishii T. T., 2004, ApJ, 604, 40

Tedesco E. F., Cellino A., Zappalá V., 2005, AJ, 129, 2869

Vaisanen P., Tollestrup E. V., Fazio G. G., 2001, MNRAS, 325, 1241

Werner M. W. et al., 2004, ApJS, 154, 1

Xu C., Lonsdale C. J., Shupe D. L., O'Linger J., Masci F., 2001, ApJ, 562, 179

SUPPLEMENTARY MATERIAL

The following supplementary material is available for this article online:

Appendix A: photometric results for simulated data

Appendix B: all-sky confusion maps

This material is available as part of the online article from http://www.blackwell-synergy.com

This paper has been typeset from a TEX/LATEX file prepared by the author.